Nanoscale

PAPER

View Article Online
View Journal | View Issue

Cite this: *Nanoscale*, 2020, **12**, 14180

Synthesis and optical properties of a $Y_3(Al/Ga)_5O_{12}$:Ce^{3+},Cr^{3+},Nd^{3+} persistent luminescence nanophosphor: a promising near-infrared-II nanoprobe for biological applications†

Luyan Wu,[a,b,c] Jie Hu,[a,b] Qilin Zou,[d] Yaling Lin,[a,b] Decai Huang,[a,b] Dejian Chen,[a,b] Hongyu Lu[a,b] and Haomiao Zhu *[a,b,c]

Persistent luminescence nanophosphors (PLNPs) emitting in the second near-infrared window (1000–1700 nm, NIR-II) are emerging as one promising class of *in vivo* bio-imaging agents due to their unique advantages including non-autofluorescence and low optical scattering in tissues. Currently, it remains a great challenge to synthesize nanosized lanthanide-doped inorganic NIR-II phosphors with a good persistent luminescence performance. Herein, we present a salt microemulsion method for synthesizing Ce^{3+}, Cr^{3+}, Nd^{3+} codoped $Y_3(Al/Ga)_5O_{12}$ nanocrystals, which generate multi-wavelength persistent luminescence in the visible (~508 nm, $5d_1 \rightarrow 4f$ of Ce^{3+}), the first near-infrared window (~890 nm, ${}^4F_{3/2} \rightarrow {}^4I_{9/2}$ of Nd^{3+}) and NIR-II (~1063 nm, ${}^4F_{3/2} \rightarrow {}^4I_{11/2}$ of Nd^{3+}) regions. Under illumination of a 410 nm diode (3 W) for 10 min, the observed duration time of NIR-II persistent luminescence is as long as 60 min at room temperature. Moreover, the persistent luminescence can be excited efficiently by multiple excitation sources including a blue diode, white LEDs and an X-ray generator, which is crucial for deep tissue imaging applications. By comparing the penetration depth between NIR-I and NIR-II persistent luminescence through chicken breast, we prove that NIR-II photons exhibit a deeper optical penetration length (3.9 mm) than that of the NIR-I ones (2.5 mm). In addition, the NIR signals can still be detected 3 min after ceasing the excitation source by a small animal imaging system (InGaAs detector) when the thickness of the covering chicken breast is 20 mm. These results show great promise for $Y_3(Al/Ga)_5O_{12}$:Ce^{3+},Cr^{3+},Nd^{3+} nanocrystals as a PLNP for bio-imaging applications with deep penetration depth and a high signal-to-noise ratio.

Received 26th April 2020,
Accepted 11th June 2020

DOI: 10.1039/d0nr03269g

rsc.li/nanoscale

Introduction

In the past decades, lanthanide or transition metal ion doped inorganic luminescent nanoparticles have been studied extensively in the fields of biomedical applications, such as biosensing,[1,2] bio-imaging[3–5] and light-triggered diagnosis and therapy,[6–8] because of their unique advantages of high emission efficiency, large Stokes shift, wide wavelength tunability, long-lived excited state, excellent chemical stability, *etc.* Despite the substantial progress that has been made so far, it still remains a great challenge to sensitively and precisely analyze complex samples due to the autofluorescence generated by the impurities or tissues, which severely interferes with the fluorescent signal of a specific target.[9–11] To overcome this problem, one approach is to utilize a time-resolved technique to filter the background fluorescence based on the advantage of the relatively long photoluminescence (PL) lifetime of trivalent lanthanide ions.[12–14] Nevertheless, extra complex apparatus is usually needed to achieve this goal.[15,16] Another promising strategy is based on the persistent luminescent nanophosphors (PLNPs), in which luminescence is maintained for an appreciable time (several seconds to days) after the excitation

---

[a] *CAS Key Laboratory of Design and Assembly of Functional Nanostructures, Fujian Key Laboratory of Nanomaterials, Fujian Institute of Research on the Structure of Matter, Chinese Academy of Sciences, Fuzhou, Fujian 350002, China. E-mail: zhm@fjirsm.ac.cn*
[b] *Xiamen Institute of Rare Earth Materials, Haixi Institute, Chinese Academy of Sciences, Xiamen, Fujian 361021, China*
[c] *University of the Chinese Academy of Sciences, Beijing 100049, China*
[d] *Centre d'Elaboration de Matériaux et d'Etudes Structurales (CEMES), CNRS, Université de Toulouse - UPS, 29 rue Jeanne Marvig, BP 94347, 31055 Toulouse, Cedex 4, France*

† Electronic supplementary information (ESI) available. See DOI: 10.1039/d0nr03269g

source is turned off, thus the undesirable autofluorescence is eliminated since continuous excitation is needless during the imaging process.[11,17–20]

The energies of the emitted photons of luminescent bioprobes have significant influence on their performance such as penetration depth. According to the wavelength, they are usually categorized as the visible, the first near-infrared window (NIR-I, 700–900 nm) and the second near-infrared window (NIR-II, 1000–1700 nm) regions, respectively.[21,22] Particularly, the probes working in the NIR-II region are of special interest due to their lower optical scattering and potential higher spatial and temporal resolution than those working in the visible or NIR-I regions in tissues, which are crucial for *in vivo* bioimaging applications.[16,23] In recent years, several NIR-I PLNPs, especially Cr^{3+}-doped gallates and gallogermanates, have been studied extensively for their synthesis, optical properties and biological applications.[24–29] The results exhibit tremendous potentiality of PLNPs as bioimaging agents with extremely high signal-to-noise ratios.[18,30–32] However, the PLNPs emitting in the NIR-II region, which are the most desired nanoprobes for *in vivo* imaging, have rarely been reported. The main obstacles may come from the limited candidates of bulk persistent luminescence phosphors in the NIR-II region and also the great challenge of synthesizing their nanosized counterparts with strong persistent luminescence. Therefore, it is highly desired to exploit new PLNPs with a long duration time of persistent luminescence in the NIR-II region, which can substantially promote the application of PLNPs in biological applications.

Yttrium aluminium garnet ($Y_3Al_5O_{12}$, YAG) with a space group of *Ia*3*d* is a famous host crystal for lanthanide doped luminescent materials such as laser crystals (*e.g.*, YAG:Nd^{3+}) and phosphors (*e.g.*, YAG:Ce^{3+}).[33–35] It has excellent chemical stability, optical isotropy and high resistance, which are pivotal for various optoelectronic applications.[33,36] Furthermore, it was found that Ce^{3+}, Nd^{3+} and Cr^{3+} codoped bulk $Y_3Al_{5-x}Ga_xO_{12}$ (YAGG, which is isostructural to that of YAG) is also a promising persistent luminescence phosphor with Nd^{3+} emissions in the NIR-I ($^4F_{3/2} \rightarrow {}^4I_{9/2}$, ~890 nm) and NIR-II ($^4F_{3/2} \rightarrow {}^4I_{11/2}$, ~1063 nm) regions. The Ce^{3+} ions in YAGG host have a strong absorption band in the visible spectral region, which means they can be excited conveniently by commercial blue light-emitting diodes (LEDs) or laser diodes. The energy in the excited state of Ce^{3+} was then captured by the electron trapping center of Cr^{3+}, and finally transferred to Nd^{3+} ions, which generate NIR persistent luminescence with a duration time of over 10 hours.[36] This outstanding persistent luminescence performance combined with the excellent chemical stability and good biological compatibility of the YAGG crystals triggered our interest towards investigating the synthesis and optical properties of YAGG:Ce^{3+},Nd^{3+},Cr^{3+} nanocrystals as well as their potentiality for bioimaging applications.

In this work, we successfully synthesized Ce^{3+}, Cr^{3+} and Nd^{3+} ion codoped YAGG nanocrystals with a particle size of about 92 nm through a salt microemulsion method.[37] The content of Ga^{3+} and doping concentrations of Ce^{3+}, Cr^{3+} and Nd^{3+} have been optimized systematically to improve the performance of NIR persistent luminescence. Finally, the longest duration time of ~60 min for the 1063 nm emission has been achieved. The underlying mechanism of the persistent luminescence was also discussed based on a variety of spectral analysis techniques, including steady, transient PL and thermoluminescence (TL) spectra. Furthermore, we evaluated the optical penetration lengths of both NIR-I and NIR-II persistent luminescence through chicken breast, and the results undoubtedly prove the superiority of NIR-II photons. These results show the great potentiality of YAGG:Ce^{3+},Cr^{3+},Nd^{3+} as a NIR-II PLNP for biological applications.

Experimental

Chemicals and materials

$Y(NO_3)_3\cdot 6H_2O$ (99.99%), $Al(NO_3)_3\cdot 9H_2O$ (99.99%), $Ga(NO_3)_3\cdot xH_2O$ (99.99%), $Ce(NO_3)_3\cdot 6H_2O$ (99.99%), $Nd(NO_3)_3\cdot 6H_2O$ (99.99%), $Cr(NO_3)_3\cdot 6H_2O$ (99.99%), urea (99%), polyethylene glycol (PEG2000), K_2SO_4 (99.99%), and Igepal CO-520 were purchased from Aladdin Chemistry, China. Cyclohexane (≥99.5%) and acetone (≥99.5%) were purchased from Sinopharm Chemical Reagent Co., Ltd, Shanghai, China. All the chemicals were used directly without further purification. The chicken breasts were purchased from a supermarket (RT-MART, Xiamen, China).

Material synthesis

The Ce^{3+}/Cr^{3+}/Nd^{3+}-doped YAGG nanocrystals were synthesized through a salt microemulsion method.[37] As an example, we give the detailed synthetic procedure for the $Y_3Al_{1.25}Ga_{3.75}O_{12}$:0.2 at% Cr^{3+},1 at% Ce^{3+},5 at% Nd^{3+} sample as follows. Firstly, 7.35 mL of $Y(NO_3)_3\cdot 6H_2O$ solution (0.4 M), 4.37 mL of $Al(NO_3)_3\cdot 9H_2O$ solution (0.4 M), 8.13 mL of $Ga(NO_3)_3\cdot xH_2O$ solution (0.4 M), 0.5 mL of $Ce(NO_3)_3\cdot 6H_2O$ solution (0.02 M), 2.5 mL of $Nd(NO_3)_3\cdot 6H_2O$ solution (0.02 M) and 0.1 mL of $Cr(NO_3)_3\cdot 6H_2O$ solution (0.02 M) were mixed with 100 mL of ultrapure water. Then 12.012 g of urea and 0.02 g of PEG2000 were added into the solution. The obtained mixture was heated to 90 °C and kept for four hours with constant stirring. After cooling down to room temperature (RT), the precipitate was collected by centrifugation and washed three times with ultrapure water.

The obtained precipitate was redispersed in 10 mL of K_2SO_4 solution (0.5 M), which was then mixed with 250 mL of cyclohexane and 25 mL of Igepal CO-520. The mixture was ultrasonicated to form a water-in-oil microemulsion. Next, 50 mL of acetone was added into the mixture and the precipitate was collected by centrifugation. The obtained powders were dried at 60 °C for 12 hours and then sintered at 1000 °C for 4 hours in air. Finally, the obtained powders were washed with water to remove K_2SO_4 residue and produce the final nanoparticles. The use of K_2SO_4 is to disperse and isolate YAGG precursors, so as to prevent the aggregation of particles during high temperature sintering because the melting point of K_2SO_4 (1067 °C) is higher than the sintering temperature.[37]

Characterization

Powder X-ray diffraction (XRD) patterns of the samples were measured using an X-ray diffractometer (MiniFlex 600, Rigaku) at an interval of 0.02° with a speed of 8° $\min^{-1}$ under Cu $K\alpha_1$ radiation (λ = 0.154187 nm). The morphology of the nanoparticles was analysed using a transmission electron microscope (TEM, FEI Talos F200S). The spectral measurements, including PL excitation and emission spectra, PL decay curves, TL curves and persistent luminescence decay curves of the samples, were carried out using a spectrometer (FLS 980, Edinburgh Instruments). The spectrometer is equipped with a continuous 450 W xenon lamp, an OPO laser (210–2600 nm, 1 kHz, NT242-1 K, EKSPLA) and two photomultiplier (PMT) detectors (PMT 1, 200–1010 nm, R2658P, HAMAMATSU; PMT 2, 950–1700 nm, H10330B-75, HAMAMATSU). The emissions in the spectral range of 450–1000 nm were recorded using PMT 1, while those in the range of 1000–1550 nm were recorded using PMT 2. A standard tungsten halogen lamp was used to correct the optical response of the spectrometer. For TL measurement, the samples were placed on a thermal stage (77–850 K, THMS 600, Linkam Scientific Instruments) to precisely control the temperature and firstly irradiated using the OPO laser (430 nm) for 10 min at 150 K. Next the samples were placed for 10 min to eliminate possible persistent luminescence and then heated up to 550 K at a heating rate of 10 K $\min^{-1}$. Meanwhile, the Ce^{3+} emission at 508 nm was monitored using PMT 1. For persistent luminescence decay curve measurements, the luminescence intensities of the samples, which have been illuminated using a 410 nm diode (3 W), a white LED (1 W) or an X-ray generator (12 W, Moxtek), were recorded at RT using PMT 1 (visible and NIR-I region) or PMT 2 (NIR-II region). To evaluate the penetration depths of the persistent luminescence in tissues, the samples were pre-excited for 10 min using a 410 nm diode (3 W) and then covered with pieces of chicken breast with various thicknesses. The NIR-I and NIR-II persistent luminescence images were taken using a small animal imaging system (Series III 900/1700, NIROPTICS) equipped with a cooled InGaAs camera (900–1700 nm). The hydrodynamic diameter and zeta potential of the synthesized nanocrystals were determined by dynamic light scattering (DLS) measurements (NanoBrook Omni, BrookHaven).

Results and discussion

Herein, we have firstly synthesized a series of YAGG:Ce^{3+},Cr^{3+},Nd^{3+} (the Ga content is fixed to x = 3.5) samples with different Ce^{3+}, Cr^{3+}, Nd^{3+} contents to determine their optimal doping concentrations by monitoring the NIR-II persistent luminescence of Nd^{3+} ions. The tried concentrations are in the range of 0.5–5 at%, 0.05–0.5 at% and 1–7 at% for Ce^{3+}, Cr^{3+} and Nd^{3+}, respectively. Finally, the achieved best combination is 1 at% of Ce^{3+}, 0.2 at% of Cr^{3+} and 5 at% of Nd^{3+}, which is adopted for all the triple doped samples. Hence, we do not indicate the specific concentrations of Ce^{3+}, Cr^{3+}, Nd^{3+} in the sample abbreviations mentioned below for brevity. Next, the content of Ga^{3+} in the YAGG host is further optimized. Fig. 1a shows the powder XRD patterns of the synthesized YAGG:Ce^{3+},Cr^{3+},Nd^{3+} nanocrystals with different Ga^{3+} contents. As we can see, all the diffraction peaks match well with the XRD pattern of YAGG (PDF#75-0556). Moreover, the diffraction peak shifts gradually to lower angles with the increasing Ga^{3+} content due to the larger ionic radius of Ga^{3+} than Al^{3+}, thus inducing the lattice expansion (Fig. 1b and c). TEM images reveal the high crystallinity of the synthesized nanoparticles with a size of ~92 nm (Fig. 1d–f; Fig. S1†). In addition, the high-resolution TEM image exhibits that the distance between the two most adjacent lattice fringes is 8.60 Å, which is corresponding to the d spacing for the (110) lattice plane of the garnet structure (Fig. 1e). The elemental mapping images confirm the presence of Y, Al, Ga, O, Ce, Cr and Nd elements in the samples (Fig. 1g).

The PL excitation and emission spectra of YAGG:Ce^{3+},Cr^{3+},Nd^{3+} nanocrystals are important to understand their basic spectral features. Fig. 2a shows the PL spectrum of the YAGG:Ce^{3+},Cr^{3+},Nd^{3+} sample (x = 3.75 of Ga) under a Xe lamp (430 nm) excitation at RT. As we can see, it is composed of multiple emission bands originated from Ce^{3+}, Cr^{3+} and Nd^{3+} ions, which cover the visible, NIR-I and NIR-II spectral regions. In the visible region, the intense emission band peaked at 508 nm is due to the $5d_1 \rightarrow 4f$ transition of Ce^{3+}. In the NIR-I region, the main emissions result from two transitions: an extremely weak emission band peaked at 690 nm of the $^2E \rightarrow {}^4A_2$ transition of Cr^{3+} ions and a number of strong emission lines around 890 nm of the $^4F_{3/2} \rightarrow {}^4I_{9/2}$ transition of Nd^{3+} ions. Most importantly, in the NIR-II region, we can observe a

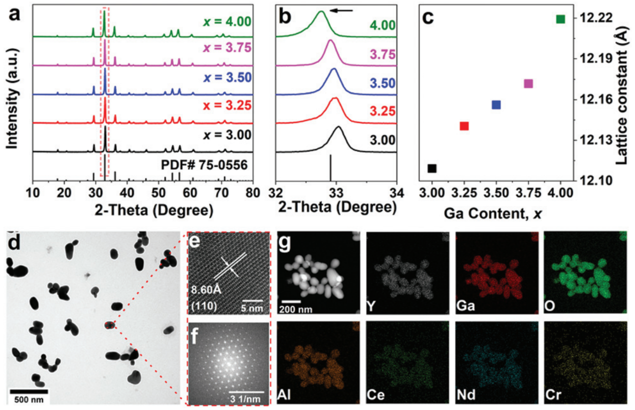

Fig. 1 (a) XRD patterns of the synthesized YAGG:Ce^{3+},Cr^{3+},Nd^{3+} (the Ga content x = 3.00, 3.25, 3.50, 3.75, 4.00) nanocrystals and the standard XRD pattern of $Y_3Al_{2.10}Ga_{2.90}O_{12}$ (PDF# 75-0556). (b) Enlarged diffraction peak in the angle range of 32° to 34°. (c) The fitted lattice constants ($a = b = c$, $\alpha = \beta = \gamma$ = 90°) of the nanocrystals with different amounts of Ga^{3+} content. (d) TEM image, (e) high-resolution TEM image and the corresponding (f) Fourier transformation pattern, and (g) the EDX elemental mapping of YAGG:Ce^{3+},Cr^{3+},Nd^{3+} (x = 3.75) nanocrystals.

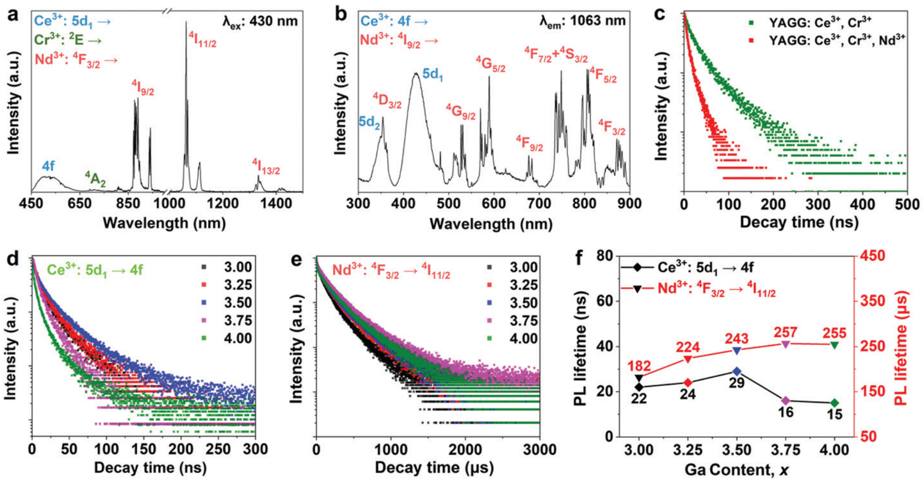

Fig. 2 (a) Photoluminescence (PL) spectra and (b) PL excitation spectra of YAGG:Ce^{3+},Cr^{3+},Nd^{3+} (x = 3.75) nanocrystals. (c) PL decay curves of Ce^{3+} (λ_{em} = 508 nm) for YAGG:Ce^{3+},Cr^{3+} (x = 3.75) and YAGG:Ce^{3+},Cr^{3+},Nd^{3+} (x = 3.75) nanocrystals. PL decay curves of (d) Ce^{3+}: $5d_1 \rightarrow 4f$ (λ_{em} = 508 nm) and (e) Nd^{3+}: $^4F_{3/2} \rightarrow {}^4I_{11/2}$ (λ_{em} = 1063 nm) as well as (f) fitted PL lifetimes of YAGG:Ce^{3+},Cr^{3+},Nd^{3+} (x = 3.00, 3.25, 3.50, 3.75, 4.00) nanocrystals.

strong emission band at 1063 nm and a relatively weak emission band at 1333 nm, which are owing to the transitions of $^4F_{3/2} \rightarrow {}^4I_{11/2}$ and $^4I_{13/2}$ of Nd^{3+} ions, respectively. The samples with other Ga^{3+} contents show similar PL spectra and are not shown here.

The PL excitation spectrum of the same sample by monitoring the 1063 nm emission of Nd^{3+} ions shows plenty of excitation bands distributed in 300–900 nm mainly from the absorption of Ce^{3+} and Nd^{3+} ions (Fig. 2b). The excitation peaks of Cr^{3+} ions are extremely weak and overlap with the strong Ce^{3+} and Nd^{3+} excitation bands, and thus are difficult to identify. From the PL emission and excitation spectra, we can conclude that there is an efficient energy transfer between Ce^{3+} and Nd^{3+} ions, because the emission of Ce^{3+} has a remarkable spectral overlap with the absorption of Nd^{3+} ions (Fig. S2†). To further deduce the energy transfer mechanism, *i.e.*, radiation reabsorption or a non-radiative energy transfer, we compare the PL decay curves of Ce^{3+} emissions between YAGG:Ce^{3+},Cr^{3+} and YAGG:Ce^{3+},Cr^{3+},Nd^{3+} nanocrystals (Fig. 2c). It can be found that after codoping with Nd^{3+} ions, the PL intensity of Ce^{3+} decay significantly faster, thus proving that the non-radiative mechanism plays a main role in the energy transfer process.

The content of Ga^{3+} ions may have a strong influence on the optical properties of YAGG:Ce^{3+},Cr^{3+},Nd^{3+} nanocrystals, especially the emission efficiency. To reveal this, we measured the PL decay curves of Ce^{3+} (508 nm) and Nd^{3+} (1063 nm) under excitation at 430 nm (OPO laser) for the YAGG:Ce^{3+},Cr^{3+},Nd^{3+} (x = 3.00, 3.25, 3.50, 3.75, 4.00) samples (Fig. 2d and e), since the excited-state dynamic decay process is sensitive to the non-radiative transition and energy transfer probability. It can be clearly seen that both the PL decay curves exhibit multi-exponential behaviour. For comparison, the average lifetimes (τ_m) were fitted by the following formula[38] and displayed *versus* the Ga content (Fig. 2f).

$$E_T = 2kT_m\left(\frac{1.26T_m}{\omega} - 1\right) \tag{1}$$

Obviously, the PL lifetime of Ce^{3+} and Nd^{3+} increases initially with the increase of the Ga content, and reach the maximum of 29 ns (Ce^{3+}) and 257 μs (Nd^{3+}) for the samples with x = 3.5 and 3.75, respectively. For the Nd^{3+} ions, this indicates that the emission efficiency of the sample with Ga content of x = 3.75 is probably the highest. While for the Ce^{3+} ions, the situation is more complicated because the decrease of lifetime may be owing to the increased non-radiative transition probability, more efficient energy transfer from Ce^{3+} to Nd^{3+} or the trap state. The non-radiative transition probability is strongly related to the structural defects with the increase of the Ga content, which act as fluorescence quenching centers. If this is the case, both Nd^{3+} and Ce^{3+} should show a decrease of lifetime when the Ga content increased from x = 3.50 to 3.75. In contrast, the PL lifetime of Nd^{3+} increased slightly. Thus, the possibility of increased non-radiative transition can be ruled out. Meanwhile, the enhanced energy transfer from Ce^{3+} to Nd^{3+} can also be excluded since the doping concentrations of Ce^{3+} and Nd^{3+} are the same for the samples with different amounts of Ga content. Therefore, the increased energy transfer from Ce^{3+} to the trap state is the most likely reason for the drastic decrease of the PL lifetime of Ce^{3+} when the Ga content increased from x = 3.50 to 3.75. This is possible if the sample with the Ga content of x = 3.75 exhibits the most intense persistent luminescence, which also means the most efficient energy transfer from Ce^{3+} to the trap state. In conclusion, the Ga content of x = 3.75 is most likely the optimal value for YAGG:Ce^{3+},Cr^{3+},Nd^{3+} nanocrystals.

Appropriate depth of the trap state (*e.g.*, the energy gap between the bottom of the conduction band and the trap state) is crucial for the generation of persistent luminescence.[17] Generally, if the trap state is too deep, the captured electrons are difficult to release using thermal activation. In contrast, if the trap is too shallow, the trapped electrons are easily released by heat and the duration time of persistent luminescence is too short for practical applications. For the YAGG:Ce^{3+},Cr^{3+},Nd^{3+} nanocrystal, the process of trapping and detrapping can be briefly described as below (Fig. S3†). Firstly, under excitation of blue light, the electrons of Ce^{3+} ions are excited from the $^2F_{5/2}$ ground state to the $5d_1$ excited-state and some of the excited electrons further jump to the conduction band by thermal activation, and then are captured by the electron trapping center of Cr^{3+}. Next, the trapped electrons are released slowly by thermal activation energy and captured by Ce^{3+} ions, which generate a broadband $5d_1 \rightarrow 4f$ transition. At the same time, some of the energy of the excited Ce^{3+} ions is transferred to the Nd^{3+} ions, thus resulting in NIR-II emissions.[36] If the excitation source is X-ray or ultraviolet light, the $^2F_{5/2}$ ground state electrons are directly excited into conduction band and then captured by the electron trapping center of Cr^{3+}. The remaining processes are the same as those under blue light excitation. From the above analysis, we can infer that the modulation of trap depth is crucial to realize efficient persistent luminescence at a desired temperature.

The Ga content in YAGG has an important effect on the depth of the trap state.[39,40] To reveal this, we measured the TL glow curves of YAGG:Ce^{3+},Cr^{3+},Nd^{3+} (x = 3.00, 3.25, 3.50, 3.75, 4.00) samples in the temperature range of 150–550 K by monitoring the 508 nm emission of Ce^{3+} ions (Fig. 3a and b). It clearly shows that the TL peak shifts to lower temperature with the increase of Ga content. Generally, the peak temperature is preferred to be at around RT, which is beneficial for the application of PLNPs in biological and medical fields. Hence, the samples with Ga contents of 3.75 (TL peaked at 290 K) and 3.50 (TL peaked at 300 K) may be the optimal choice for bioimaging applications. The depth of the trap states can be calculated by Chen's equation:[41]

$$E_T = 2kT_m\left(\frac{1.26T_m}{\omega} - 1\right), \tag{2}$$

where E_T (eV) is the trap depth; k (J K^{-1}) is the Boltzmann constant; T_m (K) is the peak temperature of the TL glow curve and ω (K) is the full width at half maximum (FWHM) of the glow peak. The calculated results are 0.204, 0.153, 0.152, 0.116 and 0.108 eV for the samples with Ga contents of x = 3.00, 3.25, 3.50, 3.75 and 4.00, respectively. It can be seen that the depth of the trap state decreases with the increase of Ga content, which is in agreement with that observed in the bulk samples reported previously.[39,40]

The performance of persistent luminescence is one of the most concerned factors for their biological applications. After being illuminated with a 410 nm diode (3 W) for 10 min, we measured the persistent luminescence decay curves of Nd^{3+} (890 nm of $^4F_{3/2} \rightarrow {}^4I_{9/2}$ and 1063 nm of $^4F_{3/2} \rightarrow {}^4I_{11/2}$) of YAGG:$Ce^{3+}$,$Cr^{3+}$,$Nd^{3+}$ (x = 3.00, 3.25, 3.50, 3.75, 4.00) samples (Fig. S4†). The results unambiguously show that the sample with Ga content of x = 3.75 shows the longest duration time. This verified the above inference that the optimal Ga content is x = 3.75 based on the PL lifetime analysis. The duration time is estimated to be 60 min for 508, 890 and 1063 nm emissions (Fig. 4a). Fig. 4b shows the persistent luminescence and the PL spectra of the YAGG:Ce^{3+},Cr^{3+},Nd^{3+} (x = 3.75) PLNPs. The positions of the emission bands for these two spectra are

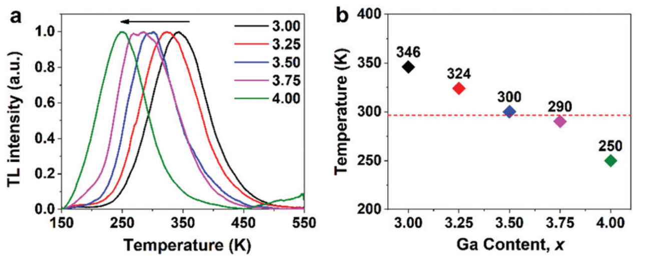

Fig. 3 (a) Thermoluminescence (TL) glow curves of YAGG:Ce^{3+},Cr^{3+},Nd^{3+} (x = 3.00, 3.25, 3.50, 3.75, 4.00) samples measured by monitoring Ce^{3+} emission at 508 nm in the range of 150–550 K. The samples were illuminated at 430 nm using an OPO laser at 150 K for 10 min and then placed for 10 min to eliminate the possible persistent luminescence. The following heating rate is 10 K min^{-1}. All the glow curves are normalized at peak temperature. (b) The peak temperature of the TL glow curves of the samples as a function of Ga content. The red dotted line represents room temperature (298 K).

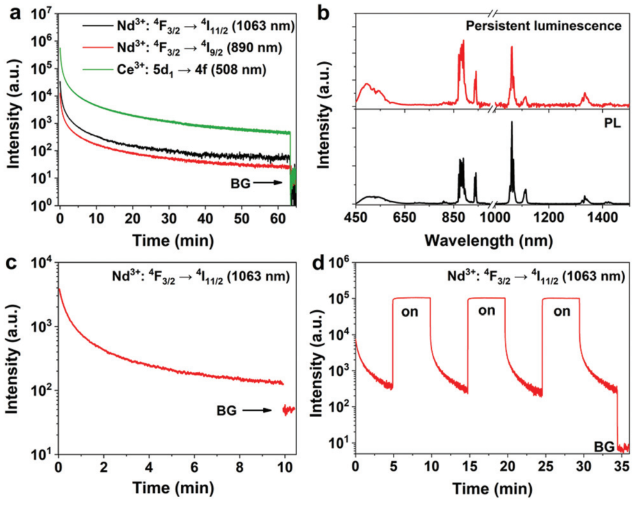

Fig. 4 (a) Persistent luminescence decay curves (λ_{em} = 508, 890 and 1063 nm) of YAGG:Ce^{3+},Cr^{3+},Nd^{3+} (x = 3.75) PLNPs after being illuminated with a 410 nm diode for 10 min. (b) Persistent luminescence and PL spectra of the YAGG:Ce^{3+},Cr^{3+},Nd^{3+} (x = 3.75) PLNPs. NIR-II persistent luminescence (λ_{em} = 1063 nm) decay curves of the YAGG:Ce^{3+},Cr^{3+},Nd^{3+} (x = 3.75) sample recorded after being illuminated by (c) a white LED (1 W) for 10 min and (d) an X-ray generator for 5 min.

essentially the same, which is reasonable since both of them are resulted from the same excited states of Ce^{3+} and Nd^{3+}.

The ability of being charged by diverse light or irradiation sources is important for the application of PLNPs. We tried to excite the YAGG:Ce^{3+},Cr^{3+},Nd^{3+} sample using a commercial compact white LED (power = 1 W) and the duration time of 1063 nm persistent luminescence is over 10 min (Fig. 4c). Another attractive irradiation source is X-ray, which has the advantage of deeper tissue penetration than those of ultraviolet or visible light, thus endowing the PLNPs with the potential ability to be recharged in deep tissue imaging applications. As shown in Fig. 4d, after being irradiated by X-ray for 5 min, the PLNPs exhibit NIR-II (1063 nm) persistent luminescence with a duration time of over 5 min. Moreover, the persistent luminescence can be activated repeatedly by X-ray and no obvious decline of the initial emission intensity was observed. These results show that YAGG:Ce^{3+},Cr^{3+},Nd^{3+} PLNPs is a promising bioimaging agent, which can be excited conveniently by multiple light sources.

As mentioned above, the optical scattering coefficient of NIR-II photons in tissues is smaller than that of the NIR-I ones. Thus, a deeper penetration of the NIR-II persistent luminescence is expected in biological tissues. To verify this, we carried out the experiments for determining the optical penetration length of YAGG:Ce^{3+},Cr^{3+},Nd^{3+} (x = 3.75) PLNPs using a small animal imaging system. The synthesized nanocrystals were covered with pieces of chicken breast with varied thicknesses (0, 1, 5 and 9 mm) and the images of persistent luminescence in NIR-I and NIR-II were taken at different delayed time periods after ceasing the excitation source, respectively. Note that a short pass optical filter (cutoff wavelength = 1000 nm) and a long pass optical filter (cut-on wavelength = 1000 nm) was used to filter the emission of PLNPs when taking the NIR-I and NIR-II images, respectively. Firstly, the PLNPs were illuminated using a 410 nm diode (3 W) for 5 min and then covered with a piece of chicken breast. Next, the images were taken after a series of fixed delayed time periods (1, 10 and 30 s) (Fig. 5a and b). We can see that the persistent luminescence intensity is decreasing with the increased thickness of chicken breast or the longer delayed time for both NIR-I and NIR-II images. It should be emphasized that the exposure time for NIR-I images (100 ms) is five times of that for NIR-II images (20 ms). The quantitative optical penetration length can be fitted by the following equation:[42,43]

$$I_\mathrm{d} = I_0 \exp[-d/L_\mathrm{p}], \tag{3}$$

where I_0 is a constant and L_p is the optical penetration length. Our fitting curves match well with the experimental data and the fitted values of L_p are 2.5 mm and 3.9 mm for NIR-I and NIR-II photons, respectively (Fig. 5c and d). Obviously, the photons in NIR-II have better penetration ability than the NIR-I ones in tissues. The optical penetration length of NIR-II emission is comparable with that of the Nd^{3+} doped LaF_3 fluorescent nanoparticles,[44] which have been successfully used for high contract *in vitro* and *in vivo* imaging in the NIR-II spectral region. In addition, when the exposure time is set to 3 s, the NIR signal can be detected 30 min and 3 min later after ceasing the excitation source when the thicknesses of chicken breast are 10 mm and 20 mm, respectively (Fig. S5†). We also tried to recharge the PLNPs, which were covered with 10 mm chicken breast, with a white LED for 5 min and the NIR persistent luminescence has been regenerated successfully (Fig. 5e). Dispersity and stability of nanocrystals in water are important for their biological applications. The magnitude of the zeta potential is usually used to evaluate the stability of nanoparticles in suspension. Generally, nanoparticles with zeta potential values greater than +30 mV or less than −30 mV have high degrees of stability.[45] To evaluate these properties, we carried out DLS measurements of the as-synthesized YAGG:Ce^{3+},Cr^{3+},Nd^{3+} nanocrystals in ultrapure water (pH = 5.6). The obtained value of zeta potential is +36.1 mV, which indicates good stability of the nanoparticles in suspension. The particle size analysis shows a single particle size distribution peak with a hydrodynamic diameter of d = 255 nm, thus proving a uniform size distribution of the YAGG nanocrystals in water (Fig. S6†). Note that the measured particle size by DLS is usually larger than that determined by TEM, because a few solvent layers may adhere to the particle surface and influence the movement of the nanoparticles.[46] In summary, all of these results show that YAGG:Ce^{3+},Cr^{3+},Nd^{3+} is a promising PLNP for biological imaging in the NIR-II spectral region.

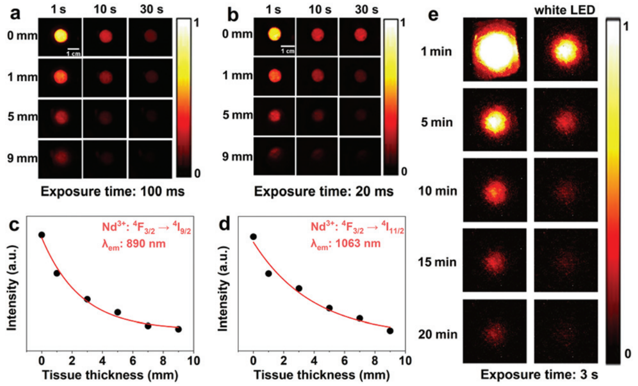

Fig. 5 (a) NIR-I and (b) NIR-II persistent luminescence images of YAGG:Ce^{3+},Cr^{3+},Nd^{3+} (x = 3.75) PLNPs covered with pieces of chicken breast with different thicknesses (0, 1, 5 and 9 mm) taken at various delayed time periods (1, 10 and 30 s) after the PLNPs being illuminated by a 410 nm diode for 5 min. The exposure time of the InGaAs camera is 100 ms and 20 ms for NIR-I and NIR-II images, respectively. Integrated (c) NIR-I and (d) NIR-II persistent luminescence intensities as a function of the thickness of chicken breast. The red line is the fitting result based on the data with a delayed time of 1 s using the eqn (2). (e) NIR persistent luminescence images of the YAGG:Ce^{3+},Cr^{3+},Nd^{3+} (x = 3.75) PLNPs covered with 1 cm-thick chicken breast taken at different delayed time periods (1, 5, 10, 15 and 20 min) after being illuminated for 5 min with a 410 nm diode (left) and the images taken after being recharged by a white LED (1 W) through the covered chicken breast (right).

Conclusions

In this work, we have successfully synthesized YAGG:Ce^{3+},Cr^{3+},Nd^{3+} nanocrystals with a particle size of ~92 nm through a salt microemulsion method. Due to the efficient energy transfer from Ce^{3+} to Nd^{3+}, the synthesized nanocrystals exhibited multiple persistent emission bands in the visible (508 nm of Ce^{3+}), NIR-I (890 nm of Nd^{3+}) and NIR-II (1063 nm of Nd^{3+}) regions. The depth of the trap state for the YAGG:Ce^{3+},Cr^{3+},Nd^{3+} samples (the Ga content x = 3.00, 3.25, 3.50, 3.75, 4.00) was observed to decrease with the increase of Ga content based on the TL glow curves. Particularly, the sample with x = 3.75 exhibited a TL glow peak of 290 K, which is close to RT and beneficial for biological applications. Finally, the optimal composition of this PLNP is determined to be $Y_3Al_{1.25}Ga_{3.75}O_{12}$:1 at% Ce^{3+},0.2 at% Cr^{3+},5 at% Nd^{3+}. Under the illumination of a 410 nm diode (3 W) for 10 min, the duration time of the 1063 nm persistent luminescence is over 60 min.

The YAGG:Ce^{3+},Cr^{3+},Nd^{3+} PLNPs can be excited conveniently by diverse excitation sources, including blue diodes, white LEDs and an X-ray generator. In particular, the deep penetration depth of X-rays is pivotal for the application of PLNPs in deep tissue imaging. The optical penetration length of persistent luminescence in the NIR-I and NIR-II regions was evaluated to be 2.5 and 3.9 mm in chicken breast, respectively. The NIR-II photons doubtlessly exhibit better penetration ability than NIR-I ones. In addition, by covering with a 20 mm chicken breast, the NIR signals can be detected 3 min after ceasing the excitation source. The DLS measurements indicated good stability of the as-synthesized nanocrystals in water. These findings show great promise for YAGG:Ce^{3+},Cr^{3+},Nd^{3+} nanocrystals as a persistent luminescence bio-imaging agent in the NIR-II region.

Conflicts of interest

There are no conflicts to declare.

Acknowledgements

This research was supported by the Priority Research Platform Project of Xiamen (no. 3502ZCQ20171002) and the Natural Science Foundation of China (no. 11804338 and 11904364). J. H. acknowledges the Chinese Academy of Sciences Pioneer "Hundred Talents Program" Young Talents (Class C).

Notes and references

1 A. Skripka, A. Benayas, R. Marin, P. Canton, E. Hemmer and F. Vetrone, *Nanoscale*, 2017, **9**, 3079–3085.

2 S. Hao, G. Chen and C. Yang, *Theranostics*, 2013, **3**, 331–345.

3 Z. Deng, X. Li, Z. Xue, M. Jiang, Y. Li, S. Zeng and H. Liu, *Nanoscale*, 2018, **10**, 9393–9400.

4 M. Kamimura, N. Kanayama, K. Tokuzen, K. Soga and Y. Nagasaki, *Nanoscale*, 2011, **3**, 3705–3713.

5 J. Shi, X. Sun, S. Zheng, J. Li, X. Fu and H. Zhang, *Biomaterials*, 2018, **152**, 15–23.

6 P. Sengar, P. Juarez, A. Verdugo-Meza, D. L. Arellano, A. Jain, K. Chauhan, G. A. Hirata and P. G. J. Fournier, *J. Nanobiotechnol.*, 2018, **16**, 19.

7 F. Wang, R. Deng and X. Liu, *Nat. Protoc.*, 2014, **9**, 1634–1644.

8 Y. Wang, H. Wang, D. Liu, S. Song, X. Wang and H. Zhang, *Biomaterials*, 2013, **34**, 7715–7724.

9 A. Abdukayum, J. T. Chen, Q. Zhao and X. P. Yan, *J. Am. Chem. Soc.*, 2013, **135**, 14125–14133.

10 M. Y. Berezin and S. Achilefu, *Chem. Rev.*, 2010, **110**, 2641–2684.

11 Q. l. M. d. Chermont, C. Chanéac, J. Seguin, F. Pellé, S. Maîtrejean, J. P. Jolivet, D. Gourier, M. Bessodes and D. Scherman, *Proc. Natl. Acad. Sci. U. S. A.*, 2007, **104**, 9266–9271.

12 Y. Gu, Z. Guo, W. Yuan, M. Kong, Y. Liu, Y. Liu, Y. Gao, W. Feng, F. Wang, J. Zhou, D. Jin and F. Li, *Nat. Photonics*, 2019, **13**, 525–531.

13 W. Zheng, S. Zhou, Z. Chen, P. Hu, Y. Liu, D. Tu, H. Zhu, R. Li, M. Huang and X. Chen, *Angew. Chem., Int. Ed.*, 2013, **52**, 6671–6676.

14 Y. Zhong, Z. Ma, F. Wang, X. Wang, Y. Yang, Y. Liu, X. Zhao, J. Li, H. Du, M. Zhang, Q. Cui, S. Zhu, Q. Sun, H. Wan, Y. Tian, Q. Liu, W. Wang, K. C. Garcia and H. Dai, *Nat. Biotechnol.*, 2019, **37**, 1322–1331.

15 D. Tu, L. Liu, Q. Ju, Y. Liu, H. Zhu, R. Li and X. Chen, *Angew. Chem., Int. Ed*, 2011, **50**, 6306–6310.

16 Y. Fan, P. Wang, Y. Lu, R. Wang, L. Zhou, X. Zheng, X. Li, J. A. Piper and F. Zhang, *Nat. Nanotechnol.*, 2018, **13**, 941–946.

17 Y. Li, M. Gecevicius and J. Qiu, *Chem. Soc. Rev.*, 2016, **45**, 2090–2136.

18 Z. Pan, Y. Y. Lu and F. Liu, *Nat. Mater.*, 2011, **11**, 58–63.

19 J. Shi, X. Sun, J. Zhu, J. Li and H. Zhang, *Nanoscale*, 2016, **8**, 9798–9804.

20 L. Song, X. H. Lin, X. R. Song, S. Chen, X. F. Chen, J. Li and H. H. Yang, *Nanoscale*, 2017, **9**, 2718–2722.

21 Y. Fan and F. Zhang, *Adv. Opt. Mater.*, 2019, **7**, 1801417.

22 Kenry, Y. Duan and B. Liu, *Adv. Mater.*, 2018, **30**, e1802394.

23 S. He, J. Song, J. Qu and Z. Cheng, *Chem. Soc. Rev.*, 2018, **47**, 4258–4278.

24 J. Wang, Q. Ma, X. X. Hu, H. Liu, W. Zheng, X. Chen, Q. Yuan and W. Tan, *ACS Nano*, 2017, **11**, 8010–8017.

25 T. Ai, W. Shang, H. Yan, C. Zeng, K. Wang, Y. Gao, T. Guan, C. Fang and J. Tian, *Biomaterials*, 2018, **167**, 216–225.

26 A. Bessière, S. Jacquart, K. Priolkar, A. Lecointre, B. Viana and D. Gourier, *Opt. Express*, 2011, **19**, 10131–10137.

27 X. H. Lin, L. Song, S. Chen, X. F. Chen, J. J. Wei, J. Li, G. Huang and H. H. Yang, *ACS Appl. Mater. Interfaces*, 2017, **9**, 41181–41187.

28 Q. Ma, J. Wang, W. Zheng, Q. Wang, Z. Li, H. Cong, H. Liu, X. Chen and Q. Yuan, *Sci. China: Chem.*, 2018, **61**, 1624–1629.

29 B. Srivastava, A. Kuang and Y. Mao, *Chem. Commun.*, 2015, **51**, 7372–7375.

30 Y. Zhuang, Y. Lv, L. Wang, W. Chen, T. L. Zhou, T. Takeda, N. Hirosaki and R. J. Xie, *ACS Appl. Mater. Interfaces*, 2018, **10**, 1854–1864.

31 Q. Lin, Z. Li and Q. Yuan, *Chin. Chem. Lett.*, 2019, **30**, 1547–1556.

32 J. Wang, Q. Ma, Y. Wang, H. Shen and Q. Yuan, *Nanoscale*, 2017, **9**, 6204–6218.

33 A. Jain, P. Sengar and G. A. Hirata, *J. Phys. D: Appl. Phys.*, 2018, **51**, 303002.

34 J. Lu, M. Prabhu, J. Song, C. Li, J. Xu, K. Ueda, A. A. Kaminskii, H. Yagi and T. Yanagitani, *Appl. Phys. B: Lasers Opt.*, 2000, **71**, 469–473.

35 M. Veith, S. Mathur, A. Kareiva, M. Jilavi, M. Zimmer and V. Huch, *J. Mater. Chem.*, 1999, **9**, 3069–3079.

36 J. Xu, S. Tanabe, A. D. Sontakke and J. Ueda, *Appl. Phys. Lett.*, 2015, **107**, 081903.

37 L. Song, Y. Dong, Q. Shao and J. Jiang, *J. Mater. Sci.*, 2018, **53**, 15196–15203.

38 Q. Tang, H. Xia, S. He, Q. Sheng and B. Chen, *Opt. Laser Technol.*, 2017, **96**, 70–75.

39 W. Li, Y. Zhuang, P. Zheng, T. L. Zhou, J. Xu, J. Ueda, S. Tanabe, L. Wang and R. J. Xie, *ACS Appl. Mater. Interfaces*, 2018, **10**, 27150–27159.

40 J. Ueda, A. Hashimoto, S. Takemura, K. Ogasawara, P. Dorenbos and S. Tanabe, *J. Lumin.*, 2017, **192**, 371–375.

41 R. Chen, *J. Appl. Phys.*, 1969, **40**, 570–585.

42 N. N. Dong, M. Pedroni, F. Piccinelli, G. Conti, A. Sbarbati, J. E. Ramírez-Hernández, L. M. Maestro, M. C. Iglesias-de la Cruz, F. Sanz-Rodriguez, A. Juarranz, F. Chen, F. Vetrone, J. A. Capobianco, J. G. Solé, M. Bettinelli, D. Jaque and A. Speghini, *ACS Nano*, 2011, **5**, 8665–8671.

43 J. Hu, D. H. Ortgies, R. A. Torres, N. Fernández, L. Porto, E. M. Rodríguez, J. G. Solé, D. Jaque, F. Alfonso and F. Rivero, *Adv. Funct. Mater.*, 2017, **27**, 1703276.

44 U. Rocha, K. U. Kumar, C. Jacinto, I. Villa, F. Sanz-Rodríguez, M. C. I. de la Cruz, A. Juarranz, E. Carrasco, F. C. J. M. van Veggel, E. Bovero, J. G. Solé and D. Jaque, *Small*, 2014, **10**, 1141–1154.

45 A. Kumar and C. K. Dixit, *Advances in Nanomedicine for the Delivery of Therapeutic Nucleic Acids*, Woodhead Publishing, 2017, pp. 43–58.

46 A. Dhawan and V. Sharma, *Anal. Bioanal. Chem.*, 2010, **398**, 589–605.